Author for correspondence:
Jiawen Luo
e-mail: jiawen.luo@erdw.ethz.ch

Optimal Kinematic Dynamos in a Sphere

Jiawen Luo[1], Long Chen[2], Kuan Li[3] and Andrew Jackson[1]

[1] Institut für Geophysik, ETH Zürich, Sonneggstrasse 5, 8092 Zürich, Switzerland
[2] Department of Mathematical Sciences, Durham University, Lower Mountjoy, Stockton Rd, Durham, DH1 3LE, UK
[3] School of Mathematics, University of Leeds, Leeds, LS2 9JT, UK

A variational optimization approach is used to optimize kinematic dynamos in a unit sphere and locate the enstrophy-based critical magnetic Reynolds number for dynamo action. The magnetic boundary condition is chosen to be either pseudo-vacuum or perfectly-conducting. Spectra of the optimal flows corresponding to these two magnetic boundary conditions are identical since theory shows that they are relatable by reversing the flow field. A no-slip boundary for the flow field gives a critical magnetic Reynolds number of 62.06, while a free-slip boundary reduces this number to 57.07. Optimal solutions are found possessing certain rotation symmetries (or anti-symmetries) and optimal flows share certain common features. The flows localize in a small region near the sphere's centre and spiral upwards with very large velocity and vorticity, so that they are locally nearly Beltrami. We also derive a new lower bound on the magnetic Reynolds number for dynamo action, which, for the case of enstrophy-normalisation, is five times larger than the previous best bound.

1. Introduction

In stars and planets, it is believed that the magnetic field is generated through motions of electrically conducting fluid in their interior. Continuous stretching and folding of the field lines sustains the magnetic field against magnetic diffusion. This process is known as the dynamo mechanism [1] and can be modeled by the set of magnetohydrodynamic (MHD) equations. The kinematic part of this subject, known as the kinematic dynamo problem, prescribes a flow field u, and asks whether there exists a seed magnetic field B_0, such that it is able to be sustained or grow exponentially with time. Motivation for this is that the magnetic field is too weak to act back on the flow at early stages of a dynamo, so the fluid momentum equation is decoupled from the magnetic field. Study of this reduced model helps us to understand how a flow field amplifies a seed magnetic field. Some flows have been found capable of sustaining dynamo action [2–5].

Although there seems to be no general criterion for a working dynamo [6], several anti-dynamo theorems were proven to exclude simple flows that cannot sustain a dynamo. Two of them are well-known. One excludes the possibility to generate a 2D magnetic field, i.e. B is either independent of any one of the Cartesian coordinates x_i or axisymmetric in spherical coordinates (also known as Cowling's theorem, see [1,7]). The other one is known as the toroidal velocity theorem which rules out dynamos maintained by purely toroidal flows in a sphere or planar flows in a Cartesian geometry [1,8,9]. These anti-dynamo theorems show that the flow field must be complex enough to create a dynamo.

A great deal of effort has been made on searching for the most efficient dynamo: [10] optimized the Kumar-Roberts flows [4]; [11] optimized a group of axially-symmetric flows based on Dudley-James flows [5] and concluded that they are close to the optimal; [12] studied a type of purely poloidal flows; [13] searched for the best dynamo among laminar ABC flows. However, all of these optimizations are carried out within a certain family of flows. A general question emerges naturally, what is the spatial structure of the optimal flow among all permissible solutions, and what ingredients constitute its optimality? This has been formulated as a variational optimization problem in a periodic box [14], in a cube [15], in a unit sphere with general flows [16] and in a unit sphere with axisymmetric flows [17]. Much efficiency has been gained by the optimal solutions compared to previous working dynamos in the sense of the magnetic Reynolds number R_m, which is a nondimensional parameter measuring the ratio between magnetic induction and diffusion.

This letter is a companion of [16] henceforth C18, in which we will report optimal solutions with different boundary conditions. The exterior of the unit sphere is considered either perfectly-conducting or with high permeability. A no-slip or free-slip boundary is used for the velocity field. Similar solutions to those of C18 are found in a no-slip setting, while solutions with a new 3-fold rotation symmetry are found in a free-slip setting. Optimal flows are localized and Beltrami-like, in the sense that u and $\nabla \times u$ are almost aligned. Various helicities are calculated. We also extend the discussion on bounds for a working dynamo given in [18].

2. Model and Method

(a) Formulation of the kinematic dynamo problem

Consider a spherical domain V filled with electrically conducting fluid. The pre-Maxwell equations simplify to a single induction equation

$$\frac{\partial \boldsymbol{B}}{\partial t} = \boldsymbol{\nabla} \times (\boldsymbol{u} \times \boldsymbol{B}) + \eta \nabla^2 \boldsymbol{B}, \tag{2.1}$$

assuming that the steady flow u is non-relativistic. Here η is the magnetic diffusivity. This equation will be nondimensionalised using the spherical radius L as a length scale, the magnetic

diffusion time $\frac{L^2}{\eta}$ as a time scale and SL as a velocity scale, where S is the root-mean enstrophy,

$$S = \sqrt{\frac{1}{V}\int_V (\boldsymbol{\nabla} \times \boldsymbol{u})^2 \, \mathrm{d}V} = \sqrt{\frac{1}{V}\int_V \boldsymbol{\omega}^2 \, \mathrm{d}V},$$ (2.2)

in which $\boldsymbol{\omega} = \boldsymbol{\nabla} \times \boldsymbol{u}$ is the vorticity. The nondimensional form of (2.1) reads

$$\frac{\partial \boldsymbol{B}}{\partial t} = R_m \boldsymbol{\nabla} \times (\boldsymbol{u} \times \boldsymbol{B}) + \nabla^2 \boldsymbol{B},$$ (2.3)

where the enstrophy-based magnetic Reynolds number is defined to be

$$R_m = \frac{SL^2}{\eta}.$$ (2.4)

The reason for adopting this definition rather than the more commonly used energy-based definition was made clear by [18]: any flow that is able to grow the magnetic field infinitely can be rescaled to a new flow with arbitrarily small kinetic energy, which still sustains a dynamo.

The linearity of (2.3) in $\boldsymbol{B}$ admits exponential solutions with a form of $\boldsymbol{B}(\boldsymbol{x}, t) = \boldsymbol{B}_0(\boldsymbol{x})e^{\gamma t}$, where $\boldsymbol{B}_0$ is an eigenvector and γ is the complex growth rate. The non-normality of (2.3) allows for a transient period at the beginning, but the eigenmode with the largest real part $Re(\gamma)$ will eventually dominate the solution. To determine whether a flow $\boldsymbol{u}$ generates a working dynamo, it suffices to check whether the magnetic field is growing or decreasing exponentially at a much longer time compared to transient phases. The growth (or decay) rate, i.e. $Re(\gamma)$, can also be calculated in such a way. For an admissible flow, the critical magnetic Reynolds number is defined to be one such that $Re(\gamma) = 0$. The critical magnetic Reynolds number R_m^c for dynamo action is defined to be

$$R_m^c := \inf_{\substack{\boldsymbol{u} \in \mathcal{D}_u \\ Re(\gamma) \geq 0}} R_m,$$ (2.5)

where $\mathcal{D}_u$ is the domain of $\boldsymbol{u}$, such that $\boldsymbol{u}$ is incompressible and satisfies any required boundary condition.

All fluid flows we consider must satisfy a non-penetration boundary condition $\hat{\boldsymbol{r}} \cdot \boldsymbol{u}|_{r=1} = 0$. We consider two extreme cases of flows, either inviscid flows that are free-slip on the boundary and thus satisfy no further condition; and viscous flows that meet a solid boundary and are thus subject to the further no-slip boundary condition $\boldsymbol{u}|_{r=1} = 0$. It would be possible to consider flows that satisfy a stress-free boundary condition, but we have not done so in our work. We expect that such flows would give an optimum slightly above the free-slip case and intermediate between the free-slip and no-slip case. Two magnetic boundary conditions are examined: pseudo-vacuum (N) and perfectly-conducting (T). A pseudo-vacuum setting is to approximate the physical conditions arising from a boundary made from very high permeability material, sometimes termed 'ferromagnetic material' [19]. This requires that the magnetic field is purely radial on the boundary, i.e. $\hat{\boldsymbol{r}} \times \boldsymbol{B}|_{r=1} = 0$. Then automatically we have $\hat{\boldsymbol{r}} \cdot (\boldsymbol{\nabla} \times \boldsymbol{B})|_{r=1} = 0$. When the fluid is surrounded by a perfect conductor, the usual assumption is that the magnetic field is zero in the perfect conductor since no current can exist [20]. Continuity of B_r requires that $\hat{\boldsymbol{r}} \cdot \boldsymbol{B}|_{r=1} = 0$. A boundary condition for $\boldsymbol{\nabla} \times \boldsymbol{B}$ can be obtained from

$$\hat{\boldsymbol{r}} \times \boldsymbol{J} = \hat{\boldsymbol{r}} \times [\sigma \boldsymbol{E} + \boldsymbol{u} \times \boldsymbol{B}].$$ (2.6)

Due to continuity of $\hat{\boldsymbol{r}} \times \boldsymbol{E}$ across the boundary and boundary conditions for $\boldsymbol{u}$, we have $\hat{\boldsymbol{r}} \times \boldsymbol{J}|_{r=1} = \hat{\boldsymbol{r}} \times (\boldsymbol{\nabla} \times \boldsymbol{B})|_{r=1} = 0$. [21] showed that there is a duality between these two magnetic boundary conditions in the sense that the spectra of the induction operator are identical. This immediately leads to the conclusion that R_m^c should be identical with both magnetic boundary conditions.

(b) Variational optimization approach

The objective function of our optimization is set to be the logarithm of the magnetic energy at a time $t = T$ (2 – 4 magnetic diffusion time in our optimization), which is long compared to the transient phases. The flow field $\boldsymbol{u}$ and initial magnetic field $\boldsymbol{B}_0$ will be optimized. Combined with the constraints on field magnitudes, solenoidal conditions and the induction equation, we build the Lagrangian as:

$$
\begin{aligned}
\mathcal{L} = {} & \ln \left\langle \boldsymbol{B}_T^2 \right\rangle - \lambda_1 \left(\left\langle (\boldsymbol{\nabla} \times \boldsymbol{u})^2 \right\rangle - 1 \right) - \lambda_2 \left(\left\langle \boldsymbol{B}_0^2 \right\rangle - 1 \right) \\
& - \langle \Pi \nabla \cdot \boldsymbol{u} \rangle - \int_0^T \left\langle p^\dagger \nabla \cdot \boldsymbol{B} \right\rangle \mathrm{d}t \\
& - \int_0^T \left\langle \boldsymbol{B}^\dagger \cdot [\partial_t \boldsymbol{B} - R_m \boldsymbol{\nabla} \times (\boldsymbol{u} \times \boldsymbol{B}) + \nabla \times \nabla \times \boldsymbol{B}] \right\rangle \mathrm{d}t \, ,
\end{aligned}
\tag{2.7}
$$

where $\langle \cdot \rangle := \frac{1}{V} \int_V \cdot \, \mathrm{d}^3 x$. In contrast to the all-space inner product used in C18, we only integrate inside the spherical domain since there is no need to include the magnetic field outside. We also switch back from the formulation in terms of Ampere's law and Faraday's law in C18 to the use of induction equation due to simplification of the magnetic boundary condition. $\boldsymbol{B}_0$ and $\boldsymbol{B}_T$ are the magnetic field at time $t = 0$ and $t = T$ respectively. λ_1, λ_2, Π, $p^\dagger$ and $\boldsymbol{B}^\dagger$ are Lagrange multipliers. The enstrophy of the flow field and the initial magnetic energy are fixed to unity.

By taking the variation of (2.7), we find the gradients of $\mathcal{L}$ with respect to $\boldsymbol{u}$ and $\boldsymbol{B}_0$:

$$
\frac{\partial \mathcal{L}}{\partial \boldsymbol{u}} = 2\lambda_1 \nabla^2 \boldsymbol{u} + R_m \int_0^T \boldsymbol{B} \times (\boldsymbol{\nabla} \times \boldsymbol{B}^\dagger) \, \mathrm{d}t + \boldsymbol{\nabla} \Pi,
\tag{2.8}
$$

$$
\frac{\partial \mathcal{L}}{\partial \boldsymbol{B}_0} = -2\lambda_2 \boldsymbol{B}_0 + \boldsymbol{B}_0^\dagger,
\tag{2.9}
$$

where the adjoint field $\boldsymbol{B}^\dagger$ is solved backward in time though the adjoint equation

$$
-\frac{\partial \boldsymbol{B}^\dagger}{\partial t} = -R_m \boldsymbol{u} \times \left(\boldsymbol{\nabla} \times \boldsymbol{B}^\dagger \right) - \boldsymbol{\nabla} \times \boldsymbol{\nabla} \times \boldsymbol{B}^\dagger + \boldsymbol{\nabla} p^\dagger
\tag{2.10}
$$

with terminal condition

$$
\boldsymbol{B}_T^\dagger = \frac{2\boldsymbol{B}_T}{\langle \boldsymbol{B}_T^2 \rangle}.
\tag{2.11}
$$

Equations (2.8) and (2.9) are used to update $\boldsymbol{u}$ and $\boldsymbol{B}_0$ iteratively. The enstrophy and initial magnetic energy are fixed to unity through the choice of λ_1 and λ_2 at each iteration. Details of the derivation and discussion of this method can be found in C18 (see also [22,23]).

(c) Numerical implementation

The induction equation (2.3) and adjoint equation (2.10) are solved using a Galerkin spectral method. $\boldsymbol{u}$ and $\boldsymbol{B}$ are expanded in spherical harmonics in the angular directions and in orthogonal polynomials in the radial direction, which satisfy the appropriate boundary conditions, see Appendix A. The procedure and examples of constructing these polynomial bases can be found in [24–26]. The divergence free property of $\boldsymbol{u}$ and $\boldsymbol{B}$ are guaranteed through a toroidal-poloidal decomposition of the vector fields. A Crank-Nicolson scheme is used for the diffusion term and a second order Adams-Bashforth scheme is used for the induction term. Numerical implementation details can be found in C18.

3. Results and Discussion

(a) Critical magnetic Reynolds number

The critical magnetic Reynolds number for dynamo action has attracted a lot of interest over the past decades. Parametric flows are optimized to numerically locate R_m^c in subclasses of $\boldsymbol{u}$, such as

Kumar-Roberts flows, Dudley-James flows and laminar ABC flows. On the other hand, various analytic lower bounds for dynamo action have also been derived. Backus [2] (see also [27]) found a bound on the maximum strain rate of the flow, which gives a bound on R_m defined in terms of the maximum strain rate; Childress [28] derived a bound for the maximum velocity; Klapper and Young [29] derived a bound for the fast dynamo growth rate involving topological enstrophy; Proctor [30] derived a lower bound of

$$\mathcal{D} \geq \frac{\pi \eta^2}{4L}, \tag{3.1}$$

where $\mathcal{D} = \int_V e_{ij} e_{ij} \, \mathrm{d}^3 x$ (e_{ij} stands for the strain rate tensor) is proportional to viscous dissipation if $\boldsymbol{u} = 0$ at ∂V. This fits into our no-slip setting, since $\mathcal{D}$ is then proportional to the enstrophy, S. Either by following the same derivation as in [30] or using definition (2.4), we are able to bound R_m by

$$R_m \geq \sqrt{\frac{3}{8}} \frac{1}{SL^2} = \sqrt{\frac{3}{8}} \approx 0.61, \tag{3.2}$$

as in C18[1].

This theoretical bound is actually far below the critical value R_m^c obtained from optimizations. We run optimizations at different R_m, starting from a random flow field and initial magnetic field, to locate the critical value R_m^c above which there exists a flow $\boldsymbol{u}$ such that the growth rate is non-negative. In C18, an insulating boundary condition is used for the magnetic field, which leads to $R_m^c \approx 64.45$. Using a pseudo-vacuum (N) or a perfectly-conducting (T) magnetic boundary condition reduces this number to 62.06 and 57.07 in no-slip and free-slip settings of $\boldsymbol{u}$ respectively. These values are at least three times lower than the best existing dynamo. We find three branches of converged solutions in the free-slip case (named with superscripts $^{(1)}$, $^{(2)}$ and $^{(3)}$, among which $^{(1)}$ is the optimum), as were found in [15]. The other two branches give slightly higher R_m^c, see Table 1.

Table 1: Basic characteristics of optimal solutions in Fig.1 and Fig.2. The critical magnetic Reynolds number R_m^c, the root-mean-square (r.m.s.) velocity $\langle \boldsymbol{u}^2 \rangle^{\frac{1}{2}}$, the vortex helicity $\langle \boldsymbol{u} \cdot \boldsymbol{\omega} \rangle$, poloidal to toroidal energy ratios (with subscript p and t) are shown. Note that the vortex helicity changes its sign under a reflection transformation since it is a pseudo-scalar. $N^{(1)}$ stands for the optimal we find in the free-slip case; $N^{(2)}$ and $N^{(3)}$ are two other converged branches, among which $N^{(2)}$ is simply a variation of the optimal found in no-slip cases. $T^{(2)}$ and $T^{(3)}$ are omitted because of the duality between the magnetic boundary conditions. 'ns' and 'fs' denote no-slip and free-slip boundary conditions respectively.

B.C.	R_m^c	$\langle \boldsymbol{u}^2 \rangle^{\frac{1}{2}}$	$\langle \boldsymbol{u} \cdot \boldsymbol{\omega} \rangle$	$\langle \boldsymbol{u}_p^2 \rangle / \langle \boldsymbol{u}_t^2 \rangle$	$\langle \boldsymbol{B}_p^2 \rangle / \langle \boldsymbol{B}_t^2 \rangle$
ns, N	62.06	0.114	0.080	1.542	0.785
ns, T	62.05	0.115	0.082	1.515	0.302
fs, $N^{(1)}$	57.07	0.155	0.117	0.789	0.819
fs, $N^{(2)}$	58.40	0.141	-0.097	1.086	0.878
fs, $N^{(3)}$	57.73	0.156	-0.112	0.757	0.989
fs, $T^{(1)}$	57.07	0.155	0.117	0.793	0.238

(b) Optimal solutions

Streamlines of the two optimal flows are shown in Fig.1a and 1b along with their spectra as a function of spherical harmonic degree l in Fig.1e and Fig.1f. Their corresponding eigenmodes with the largest growth rate are shown in Fig.2. One common feature of these two flows is that

[1] In C18 the value $\frac{\sqrt{6}}{2}$ given should read $\frac{\sqrt{6}}{4}$; the numerical value of 0.61 stated remains correct.

(a) no-slip, $|\boldsymbol{u}|$

(b) free-slip, $|\boldsymbol{u}|$

(c) no-slip, ϱ

(d) free-slip, ϱ

(e) no-slip, spectrum

(f) free-slip, spectrum
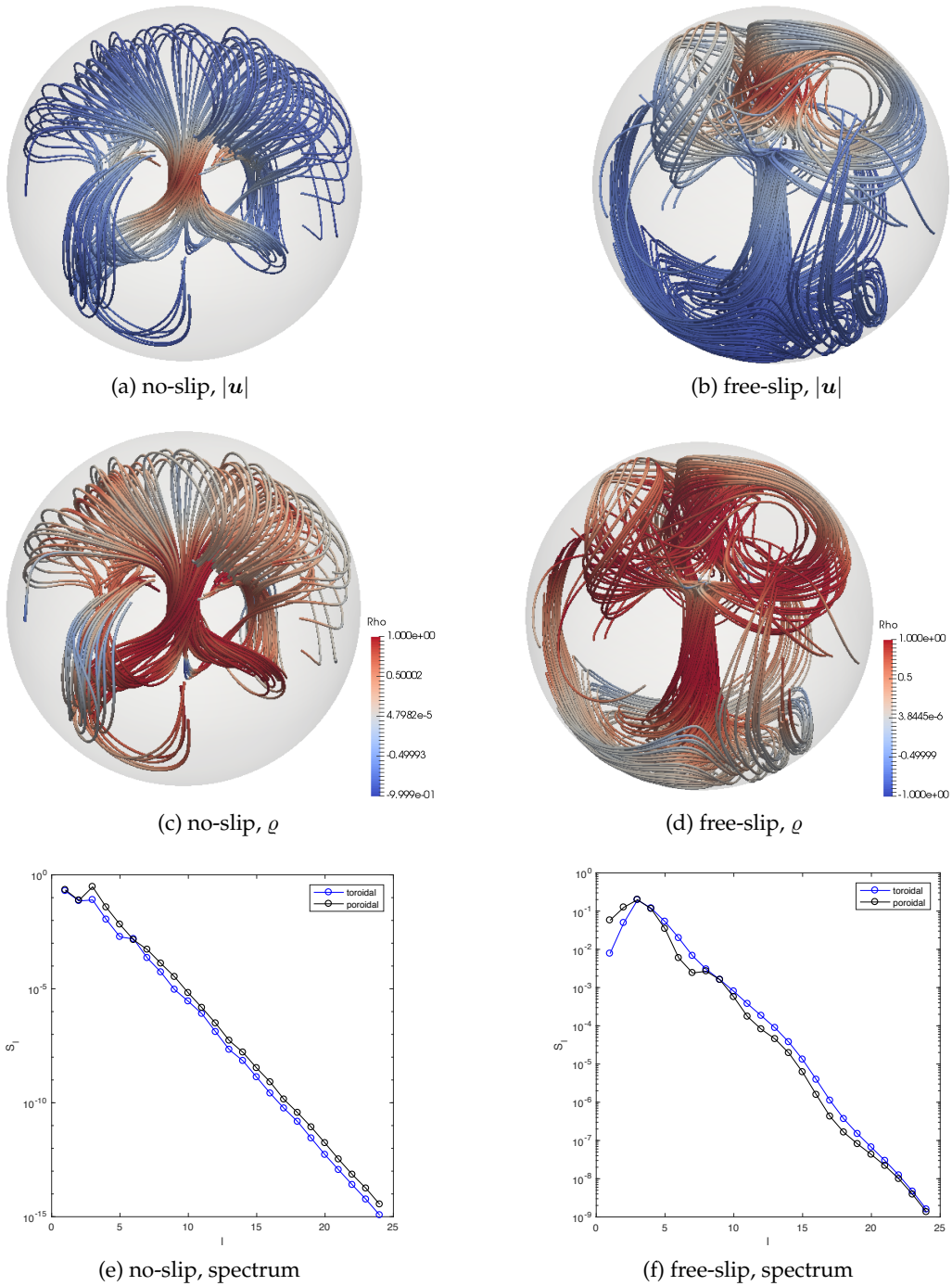
Figure 1: First row: Streamlines of optimal flows obtained when R_m is set to its critical value in each case, i.e. 62.06 and 57.07 respectively. The color scale gives velocity magnitude (red is most intense); Second row: $\rho = $ cosine of the angle between $\boldsymbol{u}$ and $\boldsymbol{\nabla} \times \boldsymbol{u}$; Third row: The spectra of $\boldsymbol{u}$ as a function spherical harmonic degree l. (a), (c), (e): no-slip; (b), (d), (f): free-slip. The axis of rotational symmetry is chosen to be vertical in (a)-(d).

they localize and spiral in a tiny region and their magnitude outside this region is quite small. In the no-slip case, two identical flow patterns spiral along with each other, while in a free-slip case there is a vertical spiraling pillar and u separates into 3 folds above it. For the optimal flow fields, we don't discriminate between two magnetic boundary conditions, since the optimum in one case will be the optimum in the other case just by by reversing it [21]. However, the eigenmodes B_T would be totally different due to different boundary conditions. The optimizations are unaware of the duality between the magnetic boundary conditions, but verified it nevertheless. Some basic characteristics are listed in Table 1. Due to the effect of the boundary condition, u has much higher poloidal to toroidal energy ratio in no-slip cases than free-slip cases. The same reasoning also applies to converting from a pseudo-vacuum boundary to a perfectly-conducting boundary.

(a) ns, N, $|\boldsymbol{B}_T|$

(b) fs, N, $|\boldsymbol{B}_T|$

(c) ns, T, $|\boldsymbol{B}_T|$

(d) fs, T, $|\boldsymbol{B}_T|$
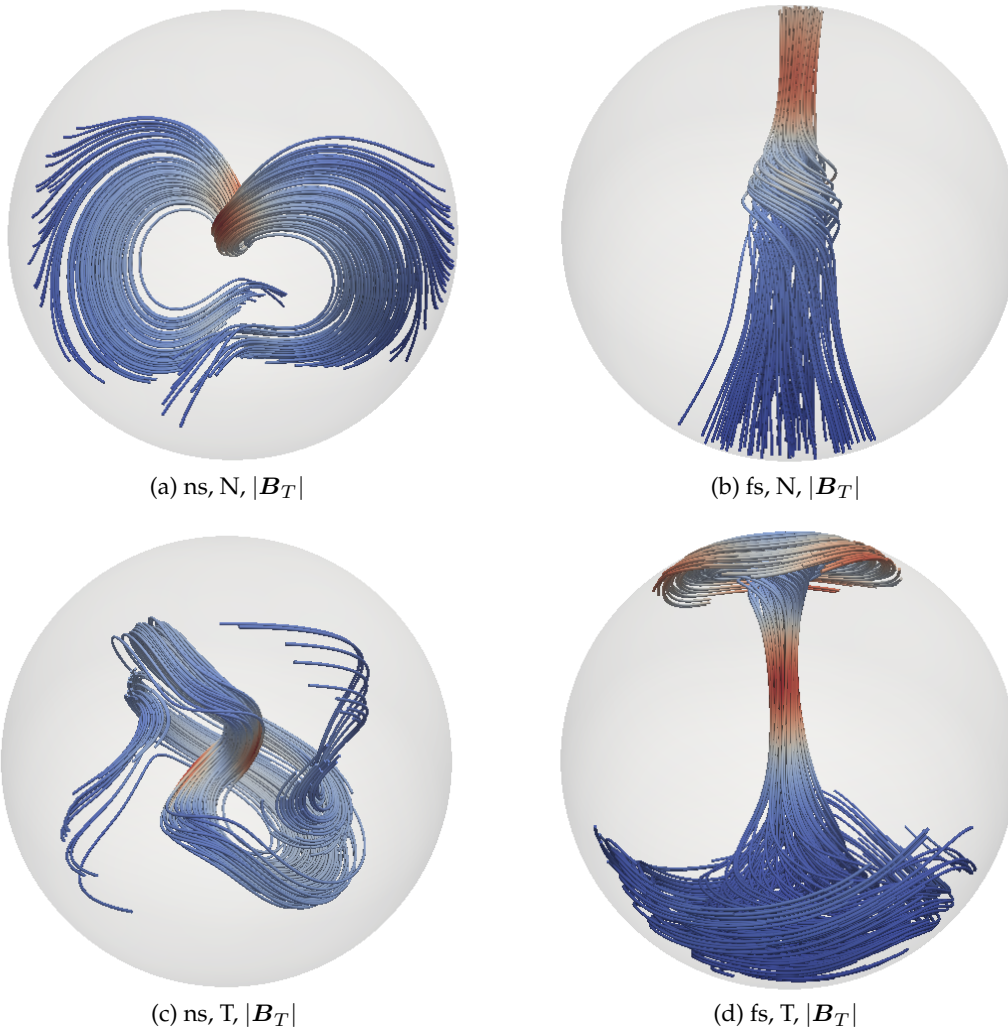
Figure 2: Field lines of eigenmodes $\boldsymbol{B}_T$ corresponding to flows in Fig.1 with different magnetic boundary conditions. 'ns' and 'fs' denote no-slip and free-slip boundary conditions for the flow respectively; N and T stand for two magnetic boundary conditions used. The color scale gives the magnetic field magnitude (red is most intense).

We find certain symmetries in the optimal solutions. In the no-slip setting, u possesses a π rotation symmetry and the two corresponding eigenmodes, $\boldsymbol{B}_T$, for N and T boundary

conditions, are anti-symmetric under the same rotation operation. When the boundary condition is changed to free-slip, the optimal $\boldsymbol{u}$ manifests itself with a 3-fold rotation symmetry, with the same for its eigenmodes. Optimal pairs $(\boldsymbol{u}, \boldsymbol{B}_T)$ are degenerate under rotation or reflection transformations, so we are allowed to rotate them such that the $z-$axis coincides with the symmetry axis. In this situation, a π rotation symmetry implies that only $m = even$ (m is the order of spherical harmonics) modes exist, while a π rotation anti-symmetry leads to only $m = odd$ modes. In the case of a 3-fold rotation symmetry, only $m = 3k$, $k \in \mathbb{N}$, modes are allowed. With a no-slip boundary condition $\boldsymbol{u}$ has a π rotation symmetry, thus by "selection rules" in [31], the magnetic field modes are separated into two independent classes, $m = even$ and $m = odd$. Our results indicate that the $m = odd$ mode gives a higher growth rate. In the case of free-slip boundary condition, $\boldsymbol{B}$ is separated into three independent classes, $m = 3k$, $m = 3k + 1$ and $3k + 2$. The first one turns out to be preferable. It is obvious that $\boldsymbol{u}$ possesses no reflectional symmetry since its mean helicity is nonzero.

Rotation of $\boldsymbol{u}$ allows us to identify its leading modes when the $z-$axis is the symmetry axis. We denote modes in the form of $\boldsymbol{u}_{l,m}^{p \text{ or } t}$, where l and m are the degree and order of spherical harmonics, p and t represent poloidal and toroidal fields respectively. In no-slip cases three modes are dominant: $\boldsymbol{u}_{1,0}^{t}$ represents a differential rotation around the symmetry axis, $\boldsymbol{u}_{1,0}^{p}$ stands for the simplest meridional circulation, and $\boldsymbol{u}_{3,2}^{p}$ represents convection rolls and non-sectorial flows. These three modes contribute about 70% of the total enstrophy. We may interpret that $\boldsymbol{u}$ consists of the simplest differential rotation and meridional circulation, coupled with complex enough higher order convective rolls. Compared to the Kumar-Roberts flow [4], in which $\boldsymbol{u}_{2,0}^{p}$ and $\boldsymbol{u}_{2,2}^{p}$ are used, the combination of $\boldsymbol{u}_{1,0}^{p}$ and $\boldsymbol{u}_{3,2}^{p}$ seems to be more effective. This is similar to the dominant modes found in C18. The optimal flows in free-slip cases have more complex structures with less dominant simple modes, and higher order components of meridional circulations are included.

(c) Helicities

The vortex helicity $h_\omega = \langle \boldsymbol{u} \cdot \boldsymbol{\omega} \rangle$ is thought to promote dynamo action by converting toroidal field into poloidal field. However, maximizing the mean helicity does not always lead to enhanced dynamo action [6] and a helical flow alone is not sufficient for dynamo action [20]. Following [32], we consider several other helicities. The mean velocity flux helicity $h_u = \langle \boldsymbol{u} \cdot \boldsymbol{a} \rangle$ is proportional to the number of linkages of flow lines, where $\boldsymbol{a}$ is the vector potential of $\boldsymbol{u}$. Since the normal component of $\boldsymbol{u}$ vanishes at the boundary, h_u is gauge-invariant. The mean cross helicity defined as $h_{B\omega} = \langle \boldsymbol{B} \cdot \boldsymbol{u} \rangle$ determines the number of linkages of magnetic force with vortex lines. Analogously, define $\zeta = \langle \boldsymbol{A} \cdot \boldsymbol{u} \rangle$, which characterizes the number of lines of magnetic force linked with flow lines. $\boldsymbol{A}$ is the magnetic vector potential and h_ζ is also gauge-invariant. Lastly, $h_B = \langle \boldsymbol{B} \cdot \boldsymbol{A} \rangle$ is known as the magnetic helicity. Among these definitions, ζ is a polar-scalar, while the others are all pseudo-scalars. Calculation of all these quantities (normalized by their upper bounds given by the Cauchy-Schwartz inequality) is shown in Table 2. Note that the values of $|h_\omega|$ are relatively high (~ 0.7 or higher). This indicates that $\boldsymbol{u}$ and $\nabla \times \boldsymbol{u}$ should be well aligned with each other.

A Beltrami flow is a flow such that

$$\nabla \times \boldsymbol{u} = \alpha \boldsymbol{u}, \tag{3.3}$$

in which α can be spatially dependent. We calculate

$$\varrho(\boldsymbol{x}) = \frac{\boldsymbol{u} \cdot (\nabla \times \boldsymbol{u})}{|\boldsymbol{u}| \cdot |\nabla \times \boldsymbol{u}|}, \tag{3.4}$$

namely the cosine of the angle between $\boldsymbol{u}$ and $\nabla \times \boldsymbol{u}$, which is shown in Fig.1c and 1d. In the no-slip case Fig.1c, $\boldsymbol{u}$ and $\nabla \times \boldsymbol{u}$ are well aligned in the central region and two extending parts below. The angle is verified to be within several degrees in these regions and even less than one degree in the most central part. In the free-slip case Fig.1d, there are also two regions where $\boldsymbol{u}$ is Beltrami like. Since these Beltrami regions are coincident with those where $\boldsymbol{u}$ has large magnitude,

Table 2: Left five columns are relative mean vortex helicity, velocity flux helicity, $\zeta = \langle \boldsymbol{A} \cdot \boldsymbol{u} \rangle$, cross helicity and magnetic helicity. Last three columns are the r.m.s. of $\boldsymbol{a}$ (vector potential of $\boldsymbol{u}$), $\boldsymbol{A}$ (vector potential of $\boldsymbol{B}$) and $\boldsymbol{u}$. Meanings of the boundary conditions can be found in Table 1.

B.C.	h_ω	h_u	ζ	$h_{B\omega}$	h_B	$\left\langle \boldsymbol{a}^2 \right\rangle^{\frac{1}{2}}$	$\left\langle \boldsymbol{A}^2 \right\rangle^{\frac{1}{2}}$	$\left\langle \boldsymbol{u}^2 \right\rangle^{\frac{1}{2}}$
ns, N	0.703	0.701	5×10^{-5}	$-4 \times 10{-4}$	-0.477	0.016	0.239	0.114
ns, T	0.711	0.713	-2×10^{-4}	-2×10^{-5}	-0.247	0.016	0.301	0.115
fs, N$^{(1)}$	0.757	0.647	-0.014	0.089	-0.562	0.028	0.262	0.155
fs, N$^{(2)}$	-0.688	-0.601	1×10^{-4}	8×10^{-4}	0.476	0.024	0.255	0.141
fs, N$^{(3)}$	-0.715	-0.578	0.026	0.059	0.505	0.030	0.252	0.156
fs, T$^{(1)}$	0.756	0.651	0.108	0.041	-0.221	0.028	0.272	0.155

we conclude that they function as engines for generation and maintenance of the magnetic field. Velocity magnitude in the outer region is much smaller and $\boldsymbol{u}$ manifests itself according to the geometry and boundary condition. Although a new flow structure appears when the boundary condition is changed from no-slip to free-slip, the critical magnetic Reynolds number does not change much. This indicates that the boundary condition on $\boldsymbol{u}$ does not significantly affect the dynamo efficiency. The magnetic boundary condition has even less effect since the optimal no-slip flows with all three magnetic boundary settings (N, T and an insulating boundary in C18) have the same spatial structure.

In Table 2, ζ and $h_{B\omega}$ are close to zero in the no-slip and N$^{(2)}$ cases due to symmetry properties of $\boldsymbol{u}$ and $\boldsymbol{B}_T$. Moreover, ζ and $h_{B\omega}$ are much smaller than h_ω, h_u and h_B. This might be a general feature for efficient dynamo actions, but requires more careful investigation. Generally speaking, none of these quantities is likely to be a single index to quantify dynamo efficiency.

4. Requirement for Dynamo Action

Although dynamo efficiency does not have a single measure, there exists analytical lower bounds for dynamo action in certain conditions. In this section we derive new analytical lower bounds for the critical magnetic Reynolds number Rm_c and compare it with our numerical solutions. We assume that the conductor is surrounded by an insulator and $\boldsymbol{u} = 0$ at the boundary $r = 1$ for simplicity. It was proved in [18] that the lower bound on R_m^c is zero when the r.m.s. velocity is fixed. This is achieved with a flow where $\boldsymbol{u}$ is almost everywhere zero, but very large in a tiny volume with concomitant steep gradients in $\boldsymbol{u}$. Let E be twice the flow energy and D be the appropriate norm for smoothness defined as

$$E = \int_V \boldsymbol{u}^2 \, \mathrm{d}^3 x \,, \qquad D = \int_V |\boldsymbol{\nabla} \boldsymbol{u}|^2 \, \mathrm{d}^3 x \,. \tag{4.1}$$

It was shown in [18] that by choosing $\boldsymbol{u}$ to be normalised such that $F_s = E^s D^{1-s} = 1$ for $0 \le s \le 1$, then if $s > \frac{1}{2}$, we have $R_m^c = 0$. Examples of this constraint are clearly that if $s = 1$, F_s constrains energy, whereas $s = 0$ constrains enstrophy. In this section we show that when $s \le \frac{1}{2}$, there exists a nonzero lower bound on R_m^c. The proof also shows that we can find bounds for higher order norms of $\boldsymbol{u}$.

From (2.3) we can derive the energy equation and bound it using Hölder's inequality

$$\frac{\mathrm{d}M}{\mathrm{d}t} = R_m \int_V (\boldsymbol{u} \times \boldsymbol{B}) \cdot (\boldsymbol{\nabla} \times \boldsymbol{B}) \, \mathrm{d}^3 x - \int_V |\boldsymbol{\nabla} \times \boldsymbol{B}|^2 \, \mathrm{d}^3 x$$

$$\le R_m \left(\int_V |\boldsymbol{u}|^q \, \mathrm{d}^3 x \right)^{\frac{1}{q}} \left(\int_V |\boldsymbol{\nabla} \times \boldsymbol{B}|^2 \, \mathrm{d}^3 x \right)^{\frac{1}{2}} \left(\int_V |\boldsymbol{B}|^p \, \mathrm{d}^3 x \right)^{\frac{1}{p}} - \int_V |\boldsymbol{\nabla} \times \boldsymbol{B}|^2 \, \mathrm{d}^3 x \,, \tag{4.2}$$

where $M = \frac{1}{2}\int_{\mathbb{R}^3} \boldsymbol{B}^2\,\mathrm{d}^3x$. The indices p and q are chosen such that

$$\frac{1}{p} + \frac{1}{q} = \frac{1}{2}, \qquad q \geq 3 \quad \text{and} \quad 2 \leq p \leq 6. \tag{4.3}$$

Using the L^p interpolation inequality, we have

$$\left(\int_V |\boldsymbol{B}|^p\,\mathrm{d}^3x\right)^{\frac{1}{p}} \leq \left(\int_V |\boldsymbol{B}|^2\,\mathrm{d}^3x\right)^{\frac{6-p}{4p}}\left(\int_V |\boldsymbol{B}|^6\,\mathrm{d}^3x\right)^{\frac{p-2}{4p}}. \tag{4.4}$$

Now an "embedding theorem" for function f sufficiently smooth and decaying fast enough at infinity is

$$\left(\int_{\mathbb{R}^3} |f|^6\,\mathrm{d}^3x\right)^{\frac{1}{6}} \leq C\left(\int_{\mathbb{R}^3} |\boldsymbol{\nabla} f|^2\,\mathrm{d}^3x\right)^{\frac{1}{2}}, \tag{4.5}$$

where the constant C has the sharpest value $(\frac{2}{\pi})^{\frac{2}{3}}3^{-\frac{1}{2}} \approx 0.4273$ [33,34]. This bounds the last integration in (4.4). In addition we have the well-known Poincaré inequality

$$\int_{\mathbb{R}^3} |\boldsymbol{B}|^2\,\mathrm{d}^3x \leq \left(\frac{1}{\pi}\right)^2 \int_V |\boldsymbol{\nabla} \times \boldsymbol{B}|^2\,\mathrm{d}^3x. \tag{4.6}$$

Since $\int_{\mathbb{R}^3} |\boldsymbol{\nabla} \boldsymbol{B}|^2\,\mathrm{d}^3x = \int_V |\boldsymbol{\nabla} \times \boldsymbol{B}|^2\,\mathrm{d}^3x$ [30], using the fact that the radial component of $\boldsymbol{B} \cdot \boldsymbol{\nabla} \boldsymbol{B}$ is continuous at the boundary (this is due to the continuity of $\boldsymbol{B}$ and $\partial_r B_r$ at the boundary), the energy growth rate can now be bounded by

$$\frac{\mathrm{d}M}{\mathrm{d}t} \leq \left[R_m \cdot C^{\frac{3p-6}{2p}}\left(\frac{1}{\pi}\right)^{\frac{6-p}{2p}}\left(\int_V |\boldsymbol{u}|^q\,\mathrm{d}^3x\right)^{\frac{1}{q}} - 1\right]\int_V |\boldsymbol{\nabla} \times \boldsymbol{B}|^2\,\mathrm{d}^3x. \tag{4.7}$$

Thus among velocity fields normalised so that $\left(\int_V |\boldsymbol{u}|^q\,\mathrm{d}^3x\right)^{1/q} = 1$, we require for dynamo action

$$R_m \geq C^{\frac{6-3p}{2p}}\pi^{\frac{6-p}{2p}}. \tag{4.8}$$

This bound is plotted in Fig. 3 as a function of q. Recall from (4.3) that $q \geq 3$. As $q \to \infty$, this bound has a limit of π, which is the same as Childress's bound with R_m defined in terms of maximum velocity, i.e. the L^∞ norm of $\boldsymbol{u}$ [28].
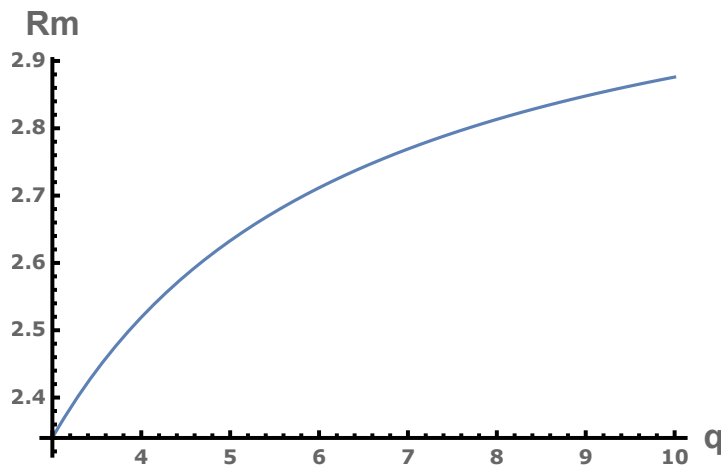

Figure 3: The lower bound of R_m given by Eq.(4.8).

Using the same argument as in (4.4) and (4.5), we have

$$\left(\int_V |\boldsymbol{u}|^q \, \mathrm{d}^3 x\right)^{2/q} \leq C^{\frac{3q-6}{q}} E^{s(q)} D^{1-s(q)} = C^{\frac{3q-6}{q}} F_{s(q)}, \tag{4.9}$$

where $s(q) = \frac{6-q}{2q} \leq \frac{1}{2}$. This proves our claim that when $s \leq \frac{1}{2}$, there exists a lower bound on R_m. Let $q = 6$, corresponding to $s = 0$ (recall this is the enstrophy-normalised case),then (4.9) gives

$$\left(\int_V |\boldsymbol{u}|^6 \, \mathrm{d}^3 x\right)^{1/6} \leq C \left(\int_V |\boldsymbol{\nabla u}|^2 \, \mathrm{d}^3 x\right)^{1/2} = C \left(\int_V |\boldsymbol{\nabla} \times \boldsymbol{u}|^2 \, \mathrm{d}^3 x\right)^{1/2}. \tag{4.10}$$

Substituting the above estimate into (4.7) gives a bound

$$R_m \geq C^{-3/2} \sqrt{3/4} = \frac{\pi}{2} 3^{3/4} \sqrt{3/4} \approx 3.1009 \tag{4.11}$$

when the normalization $\left\langle (\boldsymbol{\nabla} \times \boldsymbol{u})^2 \right\rangle = 1$ is used. This value improves the bound (3.2) by a factor of five and is also about ten times smaller than the critical R_m for transient growth found in C18, a factor suggested by [30]. The present proof is for the case of insulating boundary conditions, and an equivalent proof for other boundary conditions exists but requires a suitable amendment of (4.5) for a finite domain. We have not presented the result with this added complication.

5. Summary

In this study, we find the optimal kinematic dynamo in a sphere with various boundary conditions. A slightly smaller R_m^c is obtained compared to C18. The optimal flow in the no-slip cases turns out to be a small variation of the solution in C18, although the magnetic boundary conditions are totally different. This indicates that the magnetic boundary condition plays a secondary role compared to the flow boundary condition. In free-slip cases, a new type of solution with a 3-fold rotation symmetry has been found. Optimal flows have a common feature that they are localized in a small region where a Beltrami property is observed. This supports the view that helicity is, although not absolutely necessary, rather critical for efficient dynamo action. We also provide a new lower bound estimation of the magnetic Reynolds number for higher order ($q \geq 3$) norms of $\boldsymbol{u}$ or $F_s = E^s D^{1-s}$ with $s \leq \frac{1}{2}$.

A. Galerkin Basis

(a) The velocity field

The velocity field $\boldsymbol{u}$ is decomposed into poloidal and toroidal vectors

$$\boldsymbol{u} = \sum_{n,l,m} a_{n,l}^m \boldsymbol{t}_{n,l}^m + b_{n,l}^m \boldsymbol{s}_{n,l}^m, \tag{A 1}$$

where $\boldsymbol{t}_{n,l}^m = \boldsymbol{\nabla} \times \left(\psi_n^l(r) Y_l^m(\theta, \phi) \hat{\boldsymbol{r}} \right)$ and $\boldsymbol{s}_{n,l}^m = \boldsymbol{\nabla} \times \boldsymbol{\nabla} \times \left(\chi_n^l(r) Y_l^m(\theta, \phi) \hat{\boldsymbol{r}} \right)$ and $Y_l^m(\theta, \phi)$ are real-valued spherical harmonics fully normalised such that

$$\int_0^{2\pi} \int_0^{\pi} \left[Y_l^m \right]^2 \sin\theta \, \mathrm{d}\theta \, \mathrm{d}\phi = 1. \tag{A 2}$$

The radial basis functions $\psi_n^l(r)$ and $\chi_n^l(r)$ ($n \geq 1$) are chosen to be polynomials and constructed in terms of the Jacobi polynomials $P_n^{\alpha,\beta}(x)$, (i) in the no-slip case (first used in C18)

$$\psi_n^l(r) = r^{l+1} \left(P_n^{\left(0,l+\frac{1}{2}\right)} \left(2r^2 - 1\right) - P_{n-1}^{\left(0,l+\frac{1}{2}\right)} \left(2r^2 - 1\right) \right)$$

$$\chi_n^l(r) = r^{l+1} \sum_{i=1}^{3} c_i P_{n+2-i}^{\left(0,l+\frac{1}{2}\right)} \left(2r^2 - 1\right) \tag{A 3}$$

where

$$\begin{aligned} c_1 &= 2l + 4n + 1 \\ c_2 &= -2(2l + 4n + 3) \\ c_3 &= (2l + 4n + 5) \end{aligned} \tag{A 4}$$

and (ii) in the free-slip case

$$\phi_n^l(r) = r^{l+1} \left(c_1 P_n^{\left(0,l+\frac{1}{2}\right)} \left(2r^2 - 1\right) + c_2 P_{n-1}^{\left(0,l+\frac{1}{2}\right)} \left(2r^2 - 1\right) \right)$$

$$\chi_n^l(r) = r^{l+1} \left(1 - r^2\right) \left(c_3 P_n^{\left(1,l+\frac{1}{2}\right)} \left(2r^2 - 1\right) + c_4 P_{n-1}^{\left(1,l+\frac{1}{2}\right)} \left(2r^2 - 1\right) \right) \tag{A 5}$$

where

$$\begin{aligned} c_1 &= (2n - 1)(n + l) \\ c_2 &= -(2n + 1)(n + l + 1) \\ c_3 &= n^2(2n + 2l + 1) \\ c_4 &= -(n + 1)^2(2n + 2l + 3) \end{aligned} \tag{A 6}$$

such that after suitable normalisation, the vector modes satisfy (a) corresponding boundary conditions; (b) regularity at the origin (c) orthonormality of the form

$$\left\langle \boldsymbol{\nabla} \times \boldsymbol{s}_{n,l}^m \cdot \boldsymbol{\nabla} \times \boldsymbol{s}_{n',l'}^{m'} \right\rangle = \left\langle \boldsymbol{\nabla} \times \boldsymbol{t}_{n,l}^m \cdot \boldsymbol{\nabla} \times \boldsymbol{t}_{n',l'}^{m'} \right\rangle = \delta_{n,n'} \delta_{l,l'} \delta_{m,m'}$$

$$\left\langle \boldsymbol{\nabla} \times \boldsymbol{s}_{n,l}^m \cdot \boldsymbol{\nabla} \times \boldsymbol{t}_{n',l'}^{m'} \right\rangle = 0. \tag{A 7}$$

(b) The magnetic field

The magnetic field $\boldsymbol{B}$ is expanded in a similar manner as above

$$\boldsymbol{B} = \sum_{n,l,m} d_{n,l}^m \boldsymbol{T}_{n,l}^m + e_{n,l}^m \boldsymbol{S}_{n,l}^m, \tag{A 8}$$

where $\boldsymbol{T}_{n,l}^m = \boldsymbol{\nabla} \times \left(\Psi_n^l(r) Y_l^m(\theta, \phi) \hat{\boldsymbol{r}} \right)$ and $\boldsymbol{S}_{n,l}^m = \boldsymbol{\nabla} \times \boldsymbol{\nabla} \times \left(\Upsilon_n^l(r) Y_l^m(\theta, \phi) \hat{\boldsymbol{r}} \right)$. The radial basis functions $\Psi_n^l(r)$ and $\Upsilon_n^l(r)$ ($n \geq 1$) are constructed as (i) in the pseudo-vacuum (N) case (first used

in [23])

$$\Psi_n^l(r) = r^{l+1}\left(1 - r^2\right) P_{n-1}^{\left(2, l+\frac{1}{2}\right)}\left(2r^2 - 1\right)$$

$$\Upsilon_n^l(r) = r^{l+1}\left(c_1 P_n^{\left(0, l+\frac{1}{2}\right)}\left(2r^2 - 1\right) + c_2 P_{n-1}^{\left(0, l+\frac{1}{2}\right)}\left(2r^2 - 1\right)\right)$$

(A 9)

where

$$c_1 = (2n - 1)(n + l)$$

$$c_2 = -(2n + 1)(n + l + 1).$$

(A 10)

and (ii) in the perfectly-conducting (T) case

$$\Psi_n^l(r) = r^{l+1}\left(c_1 P_n^{\left(2, l+\frac{1}{2}\right)}\left(2r^2 - 1\right) + c_2 P_{n-1}^{\left(2, l+\frac{1}{2}\right)}\left(2r^2 - 1\right) + c_3 P_{n-2}^{\left(2, l+\frac{1}{2}\right)}\left(2r^2 - 1\right)\right)$$

$$\Upsilon_n^l(r) = r^{l+1}\left(c_4 P_{n+1}^{\left(1, l+\frac{1}{2}\right)}\left(2r^2 - 1\right) + c_5 P_n^{\left(1, l+\frac{1}{2}\right)}\left(2r^2 - 1\right) + c_6 P_{n-1}^{\left(1, l+\frac{1}{2}\right)}\left(2r^2 - 1\right)\right).$$

(A 11)

Note that the last term in the definition of $\Psi_n^l(r)$ should be ignored when $n = 1$. The coefficients are defined as

$$c_1 = n(4n + 1 + 2l)(2n + 5 + 2l)$$
$$(8l^2 n^2 + 16ln^3 + 8n^4 + 8ln^2 + 8n^3 - 2l^2 - 10ln - 8n^2 - 2l - 5n + 3)$$
$$c_2 = -2(4n + 3 + 2l)(16l^3 n^3 + 48l^2 n^4 + 48ln^5 +$$
$$16n^6 + 24l^3 n^2 + 120l^2 n^3 + 168ln^4 + 72n^5 - 4l^3 n + 60l^2 n^2 + 164ln^3 + 100n^4 -$$
$$6l^3 - 30l^2 n + 6ln^2 + 30n^3 - 21l^2 - 44ln - 26n^2 - 15l - 12n)$$
$$c_3 = (n + 1)(2n - 1 + 2l)(4n + 5 + 2l)$$
$$(8l^2 n^2 + 16ln^3 + 8n^4 + 16l^2 n + 56ln^2 + 40n^3 + 6l^2 + 54ln + 64n^2 + 12l + 35n + 6)$$
$$c_4 = (4n + 2l + 3)(4ln + 4n^2 + 2l + 6n - 1)n$$
$$c_5 = -4n(n + 2)(4n + 5 + 2l)(2n + 3 + 2l)$$
$$c_6 = (n + 2)(4n + 2l + 7)(4ln + 4n^2 + 6l + 14n + 9).$$

(A 12)

Similarly, these vector modes defined above, after suitable normalisation, satisfy (a) corresponding boundary conditions; (b) regularity at the origin (c) orthonormality of the form

$$\left\langle \boldsymbol{S}_{n,l}^m \cdot \boldsymbol{S}_{n',l'}^{m'}\right\rangle = \left\langle \boldsymbol{T}_{n,l}^m \cdot \boldsymbol{T}_{n',l'}^{m'}\right\rangle = \delta_{n,n'}\delta_{l,l'}\delta_{m,m'}$$

$$\left\langle \boldsymbol{S}_{n,l}^m \cdot \boldsymbol{T}_{n',l'}^{m'}\right\rangle = 0.$$

(A 13)

References

1. Moffatt HK. 1978 Field generation in electrically conducting fluids. *Cambridge University Press, Cambridge, London, New York, Melbourne* **2**, 5–1.
2. Backus G. 1958 A class of self-sustaining dissipative spherical dynamos. *Annals of Physics* **4**, 372–447.
3. Pekeris CL, Accad Y, Shkoller B. 1973 Kinematic Dynamos and the Earth's Magnetic Field. *Philosophical Transactions of the Royal Society A: Mathematical, Physical and Engineering Sciences* **275**, 425–461.
4. Kumar S, Roberts PH. 1975 A Three-Dimensional Kinematic Dynamo. *Proceedings of the Royal Society A: Mathematical, Physical and Engineering Sciences* **344**, 235–258.

5. Dudley ML, James RW. 1989 Time-Dependent Kinematic Dynamos with Stationary Flows. *Proceedings of the Royal Society A: Mathematical, Physical and Engineering Sciences* **425**, 407–429.

6. Gubbins D. 2008 Implication of kinematic dynamo studies for the geodynamo. *Geophysical Journal International* **173**, 79–91.

7. Cowling TG. 1933 The magnetic field of sunspots. *Monthly Notices of the Royal Astronomical Society* **94**, 39–48.

8. Elsasser WM. 1946 Induction Effects in Terrestrial Magnetism Part I. Theory. *Physical Review* **69**, 106–116.

9. Proctor M. 2004 An extension of the Toroidal Theorem. *Geophysical & Astrophysical Fluid Dynamics* **98**, 235–240.

10. Love JJ, Gubbins D. 1996 Optimized kinematic dynamos. *Geophysical Journal International* **124**, 787–800.

11. Holme R. 2003 Optimised axially-symmetric kinematic dynamos. *Physics of the Earth and Planetary Interiors* **140**, 3–11.

12. Love JJ, Gubbins D. 1996 Dynamos driven by poloidal flow exist. *Geophysical Research Letters* **23**, 857–860.

13. Alexakis A. 2011 Searching for the fastest dynamo: Laminar ABC flows. *Physical Review E* **84**.

14. Willis AP. 2012 Optimization of the Magnetic Dynamo. *Physical Review Letters* **109**.

15. Chen L, Herreman W, Jackson A. 2015 Optimal dynamo action by steady flows confined to a cube. *Journal of Fluid Mechanics* **783**, 23–45.

16. Chen L, Herreman W, Li K, Livermore PW, Luo JW, Jackson A. 2018 The optimal kinematic dynamo driven by steady flows in a sphere. *Journal of Fluid Mechanics* **839**, 1–32.

17. Holdenried-Chernoff D, Chen L, Jackson A. 2019 A trio of simple optimized axisymmetric kinematic dynamos in a sphere. *Proceedings of the Royal Society A* **475**, 20190308.

18. Proctor M. 2015 Energy requirement for a working dynamo. *Geophysical & Astrophysical Fluid Dynamics* **109**, 611–614.

19. Jackson A, Sheyko A, Marti P, Tilgner A, Cébron D, Vantieghem S, Simitev R, Busse F, Zhan X, Schubert G, et al.. 2013 A spherical shell numerical dynamo benchmark with pseudo-vacuum magnetic boundary conditions. *Geophysical Journal International* **196**, 712–723.

20. Jones CA. 2008 pp. 45–135. In *Course 2 Dynamo theory*, pp. 45–135. Elsevier.

21. Favier B, Proctor MRE. 2013 Growth rate degeneracies in kinematic dynamos. *Physical Review E* **88**.

22. Kerswell RR, Pringle CCT, Willis AP. 2014 An optimization approach for analysing nonlinear stability with transition to turbulence in fluids as an exemplar. *Reports on Progress in Physics* **77**, 085901.

23. Li K, Jackson A, Livermore PW. 2011 Variational data assimilation for the initial-value dynamo problem. *Physical Review E* **84**.

24. Livermore P. 2014 A Compendium of Galerkin Orthogonal Polynomials (2014). *URL http://homepages.see.leeds.ac.uk/earpwl/Galerkin/Galerkin.html, accessed*.

25. Livermore PW. 2010 Galerkin orthogonal polynomials. *Journal of Computational Physics* **229**, 2046–2060.

26. Livermore PW, Ierley GR. 2009 Quasi-L^p norm orthogonal Galerkin expansions in sums of Jacobi polynomials. *Numerical Algorithms* **54**, 533–569.

27. Proctor MRE. 1977 On Backus' necessary condition for dynamo action in a conducting sphere. *Geophysical & Astrophysical Fluid Dynamics* **9**, 89–93.

28. Childress S. 1969 Théorie magnetohydrodynamique de l'effet dynamo. *Report, Department of Mechanics, Faculty of Science, University of Paris*.

29. Klapper I, Young LS. 1995 Rigorous bounds on the fast dynamo growth rate involving topological entropy. *Communications in Mathematical Physics* **173**, 623–646.

30. Proctor MRE. 1979 Necessary conditions for the magnetohydrodynamic dynamo. *Geophysical & Astrophysical Fluid Dynamics* **14**, 127–145.

31. Bullard E, Gellman H. 1954 Homogeneous Dynamos and Terrestrial Magnetism. *Philosophical Transactions of the Royal Society A: Mathematical, Physical and Engineering Sciences* **247**, 213–278.

32. Ruzmalkln AA, Sokoloff DD. 1980 Helicity, linkage and dynamo action. *Geophysical & Astrophysical Fluid Dynamics* **16**, 73–82.

33. Rosen G. 1971 Minimum Value for c in the Sobolev Inequality $\|\phi^3\| \le c\|\nabla\phi\|^3$. *SIAM Journal on Applied Mathematics* **21**, 30–32.

34. Talenti G. 1976 Best constant in Sobolev inequality. *Annali di Matematica Pura ed Applicata, Series 4* **110**, 353–372.